International Journal of Ocean Engineering and Technology Vol. 4, No. 1, pp 1~9, April 2001 (ISSN 1229-1668)

Large Amplitude Heave and Roll Simulations by the Chimera RANS Method

CHANG-HO KANG
J. Ray McDermott Engineering, LLC, USA
(Received 25 February 2001, accepted 7 April 2001)

ABSTRACT: *An oscillating body motion with extremely large amplitude has been studied using the viscous flow solver. Time simulations of oscillating ship hull in prescribed heave and roll motions are presented using RANS method with FAM approach (Chen,1995). For viscous flows, laminar flow and turbulent flow with $k-\varepsilon$ model are considered and compared. The viscous flow solver of RANS method is performed together with a Chimera type of multi-block grid system to demonstrate the advantage of accurate and efficient zonal approach. In the present study, effects of viscosity and oscillation degree are discussed using Re=1000 and Re=1000000. Large motion of oscillating body shows clear vortex propagation that is not possible for inviscid flow to present.*

KEY WORDS: RANS, Chimera, FAM, nonlinear waves, viscous flows, heave, roll.

1. Introduction

In the past decade, the simulation of ocean floating structure has been very important subject in industry. Many attempts have been made to interpret the qualitative behavior of the floating structure motion and caused fluid flow. The ocean floating structure may include spar buoy, TLP (Tension Leg Platform), semi-submersibles and FPSO (Floating Production, Storage and Offloading). The analyses of motion and load responses about these structures have been focused on deep water industry for oil production and storage. Previously, small motion simulation was concentrated using frequency linear approach due to slow computers and low memory capacity. Due to advanced computer technology, people have moved to large amplitude nonlinear motion analysis.

In the study of body-fluid problems, a potential flow method is usually applied due to well-developed theory. Although this potential flow theory is basic and essential to rough estimation of floating structure design before construction, the theory has difficulty in capturing some more detailed flow phenomena such as wakes, flow separation, roll damping, and vortex shedding in case of extreme condition. Because of disadvantage of capturing viscous flow phenomena, the potential method has utilized pre-captured empirical formulas. However, the laboratory can not test every cases for these empirical formula, and so the potential method has critical limitation in that sense. In order to overcome the drawback, the well-formed viscous flow solver is required. Currently presented Chimera RANS method may hope to solve the large motion analyses including vortex shedding and precise damping effect.

Prescribed or freely floating body motion has been investigated by many researchers over past several decades. Wu (Wu, 1990) and Yeung and Wu (Yeung, 1991) carried out linearized Navier Stokes equations to consider a small oscillating body in a viscous fluid. Isaacson and Cheung (Isaacson, 1991; 1992) and Isaacson and Ng (Isaacson, 1993) presented a time-domain second-order method to study the nonlinear wave diffraction and radiation problems utilizing a boundary integral equation method. Taneda (Taneda, 1991) observed the flow around a half-submerged oscillating sphere. Yeung and Ananthakrishnan (Yeung, 1992) considered the heaving cylinder motion in viscous flow using the fractional-step method. The coupled heave-roll motions of a vessel in head or following sea conditions are studied using a nonlinear model by Liaw et al (Liaw, 1993). Recently, the RANS method of Chen, Kang, and Huang (Chen, 1998) has been utilized to incorporate a flexible Chimera domain decomposition technique for roll motion simulation of ship hull body.

In the present study, the RANS method has been further utilized to investigate extremely large heave and roll motions of the floating body. Both laminar and turbulent flows are considered with interactive Chimera multi-block grid system. For the turbulent flows, a two-layer - turbulence model (Chen, 1988; 1989) is employed. The governing equations for momentum and turbulence quantities are solved using the FAM method (Chen, 1990). The coupling between the pressure and velocity in the FAM method is accomplished using a hybrid Semi-Implicit Method for Pressure-Linked Equations Revised (SIMPLER) and Pressure-Implicit with Splitting of Operators (PISO) algorithm (Chen, 1989; 1993). From large motion of the body in current simulation, more accurate flow behavior around the body has been investigated. The effect of Reynolds number and amplitude of heave and roll motions is

investigated in the current study.

2. RANS Method

In the present study, the Chimera RANS method of Chen, Chen and Davis (Chen, 1997) has been employed in the vicinity of the body for accurate resolution of the unsteady, viscous flows induced by the body motions. The method solves the nondimensional Reynolds-Averaged Navier-Stokes equations for incompressible flow in orthogonal curvilinear coordinates $(x^i,t)=(x^1,x^2,x^3,t)$:

$$\frac{\partial U_i}{\partial x_i}=0 \tag{1}$$

$$\frac{\partial U_i}{\partial t}+U_j\frac{\partial U_i}{\partial x_j}+\frac{\partial \overline{u_iu_j}}{\partial x_j}+\frac{\partial p}{\partial x_i}-\frac{1}{Re}\nabla^2U_i=0 \tag{2}$$

where U_i and u_i represent the mean and fluctuating velocity components. t is time, p is pressure, and $Re=U_0L/\nu$ is the Reynolds number based on a characteristic length L, a reference velocity U_0, and the kinematic viscosity ν. The reference lengths used in the current study are half beam or draft. The reference velocities are maximum velocities of prescribed motion including heave or roll. Eq. (1) represents the continuity equation and Eq. (2) represents the mean momentum equation. The equations are written in tensor notation with the usual summation convention assumed. In the present study, the two-layer turbulence model of Chen and Patel (Chen, 1988) is employed to provide closure for the Reynolds stress tensor $\overline{u_iu_j}$.

In the transformed plane (ξ^i,τ), the equation of continuity and the transport equation for momentum and turbulence quantities can be written as, respectively:

$$\frac{1}{J}\frac{\partial}{\partial\xi^i}(b^i{}_jU_j)=0 \tag{3}$$

and

$$\frac{\partial\Phi}{\partial\tau}+\left[(U_j-W_j)\xi^k_{,j}+\frac{1}{R_\Phi}f^k\right]\frac{\partial\Phi}{\partial\xi^k}+\left[S_\Phi+\frac{1}{R_\Phi}g^{ij}\frac{\partial^2\Phi}{\partial\xi^i\partial\xi^j}\right]=0 \tag{4}$$

where W_j is the grid velocity of the moving grid. The effective Reynolds number is defined by

$$\frac{1}{R_\Phi}=\frac{1}{Re}+\frac{\nu_t}{\sigma_\Phi} \tag{5}$$

Here, physical variables Φ are $\Phi=(U_i,k,\varepsilon)$ and $\xi^k_{,j}$ is the inverse of the covariant transformation tensor $\frac{\partial x^k}{\partial\xi^j}$. The modeling constants used in the current study are $\sigma_\Phi=(\sigma_{U_i},\sigma_k,\sigma_\varepsilon)=(1,1,1.3)$. Several source terms are collected as:

$$S_{U_i}=\frac{1}{J}b_i^j\frac{\partial}{\partial\xi^j}\left(p+\frac{2}{3}k\right)+\frac{1}{J}\left\{\frac{1}{J}b_j^kb_i^m\frac{\partial\nu_t}{\partial\xi^k}\frac{\partial U_j}{\partial\xi^m}\right\} \tag{6}$$

$$S_k=-G+\varepsilon \tag{7}$$

$$S_\varepsilon=-\frac{\varepsilon}{k}(C_{\varepsilon1}G)+C_{\varepsilon2}\frac{\varepsilon^2}{k} \tag{8}$$

The metric and conjugate metrics coefficients are defined by, respectively

$$g_{ij}=\frac{\partial x^m}{\partial\xi^i}\frac{\partial x^m}{\partial\xi^j} \tag{9}$$

$$g^{li}=\frac{1}{g}(g_{mj}g_{nk}-g_{mk}g_{nj}) \tag{10}$$

where

$$g=J^2=g_{11}g_{22}g_{33}+2g_{12}g_{13}g_{23}-(g_{23})^2g_{11}-(g_{13})^2g_{22}-(g_{12})^2g_{33} \tag{11}$$

Here, indices (l,m,n) and (i,j,k) are in cyclic order. Other geometric coefficients are defined as:

$$f^k=\nabla^2\xi^k=\frac{1}{J}\frac{\partial}{\partial\xi^l}(Jg^{kl})=\frac{1}{J}\frac{\partial}{\partial\xi^l}(Jb_m^kb_m^l) \tag{12}$$

$$b_i^l=J\frac{\partial\xi^l}{\partial x^i}=\frac{\partial x^j}{\partial\xi^m}\frac{\partial x^j}{\partial\xi^n}-\frac{\partial x^j}{\partial\xi^m}\frac{\partial x^j}{\partial\xi^n} \tag{13}$$

The production term G and other terms are explained in detail in Kang (Kang, 1998). The modeling constants in the present study are $C_{\varepsilon1}=1.44$ and $C_{\varepsilon2}=1.92$.

On the free surface, the viscosity and surface tension are neglected in the current viscous flow study. The free surface kinematic boundary condition (FSKBC) and the free surface dynamic boundary condition (FSDBC) can be expressed as, respectively.

$$\delta_\tau=w-(\delta_\xi\xi_x+\delta_\eta\eta_x)u-(\delta_\xi\xi_y+\delta_\eta\eta_y)v \tag{14}$$

and

$$\frac{\partial U_i}{\partial n}=0 \quad \text{and} \quad p=\frac{\delta}{Fr^2} \tag{15}$$

Here, δ is free surface elevation. Note that the pressure in FSDBC in Eq. (15) and all the pressures below the free surface boundary are dynamic pressure.

The far field boundary condition in the viscous flow is using zero normal gradient boundary condition

$$\frac{\partial U_i}{\partial n}=0 \quad \text{and} \quad \frac{\partial p}{\partial n}=0 \tag{16}$$

This far field boundary condition is employed with the damping zone[17] to prevent possible wave reflection from far field boundary in the current study. The zero normal gradient boundary condition (Eq. (16)) in the viscous flow may not be sufficient to prevent reflection at the far field. In the current study, a damping zone is applied together with the zero normal gradient boundary condition. The artificial damping factor applied at the damping zone is

$$\alpha=\left(0,0,-0.5\left(\frac{\eta-\eta_S}{\eta_E-\eta_S}\right)^2\left(\frac{\zeta-\zeta_B}{\zeta_F-\zeta_B}\right)\right)\cdot(u,v,w) \tag{17}$$

where $\eta_S \le \eta \le \eta_E$ and $\zeta_B \le \zeta \le \zeta_F$. η_S and η_E are the start and end points in the transformed coordinate in the direction of η, while ζ_B and ζ_F are the bottom and free surface points in the transformed coordinate in the direction of ζ. η and ζ directions represent the horizontal and vertical directions in rectangular grid system, respectively.

The moving body boundary condition for the viscous flow is relatively simple compared to that for the potential flow. A no-slip boundary condition is applied on the body surfaces. In other words, fluid particles move with the body at the same velocity.

$$U_i|_{Fluid}=V_i|_{Body} \tag{18}$$

The bottom or fixed body boundary condition can be simply obtained with $U_i|_{Fluid}=0$ in Eq. (18). The pressure at the floating body or bottom is extrapolated near body or bottom points. Since a dense grid is used around the body, the error due to the extrapolation should be negligible.

In the viscous flow, the no-slip boundary condition is usually applied to the body surface except for the intersection points. The no-slip boundary is inconsistent with the free surface boundary condition at the body and free surface intersection. Due to inconsistency, the slip boundary condition is applied at the intersection. This slip boundary condition may result in the zero normal velocity on the free surface around the body. Since the minimum grid spacing normal to the body is small, the error due to this zero normal velocity should be correspondingly small, hence comparable with other discretization errors.

3. Numerical Method

The present FAM method combines a two-dimensional local analytic solution in the $\eta\zeta$ plane with a one-dimensional local analytic solution in the ξ direction that aligned roughly with the primary flow direction. In the finite-analytic approach, the governing transport equation is locally linearized in each rectangular numerical element, $\Delta\xi=\Delta\eta=\Delta\zeta=1$ by evaluating the coefficients at the interior node (P) of each local element. Details in the FAM are described in Chen et al (Chen, 1990), and the following is the final twelve points in FAM formula for the equation as shown in Fig. 1.

$$\Phi_P=\frac{1}{1+C_P\left[C_U+C_D+R_\Phi/\Delta\tau\right]}\left\{\sum_1^8 C_{nb}\Phi_{nb}+C_P\left(C_U\Phi_U+C_D\Phi_D+\frac{R_\Phi}{\Delta\tau}\Phi_P^{n-1}\right)-C_P(S_\Phi)_P\right\} \tag{19}$$

where

$$\sum_1^8 C_{nb}\Phi_{nb}=C_{NE}\Phi_{NE}+C_{NW}\Phi_{NW}+C_{SE}\Phi_{SE}+C_{SW}\Phi_{SW}+C_{NC}\Phi_{NC}+C_{SC}\Phi_{SC}+C_{EC}\Phi_{EC}+C_{WC}\Phi_{WC}$$

Here, subscript nb denotes neighboring nodes (NE: northeast, NW: northwest, etc.). After simultaneous algebraic tri-diagonal equations have been formulated from FAM formula, iterative

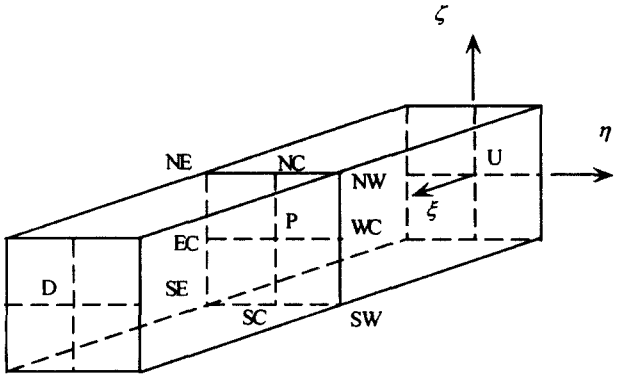

Fig. 1 Finite analytic local element

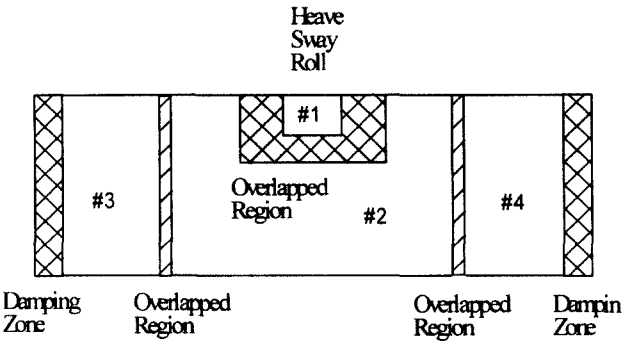

Fig. 2 Chimera grid system for prescribed motion

Alternating Direct Implicit (ADI) is used to solve those equations.

The grid system in the Chimera method is a multi-block system that is composed of several structured grid blocks. This multi-block system is more efficient for complex geometry including relative motions. The present floating body grid system is shown in Fig. 2. For convenience, two different grid systems are used concurrently in the present study: One is a simple grid system representing the wave tank where only the free surface is allowed to move. The other is a floating body grid system that can be moved in arbitrary combinations of translational and rotational motions.

The floating body grids have two kinds of system: one is called baseline grid system that is allowed to move only and not to regrid. The other one is regenerated grid from baseline grid when it finishes moving to final position. The baseline grid (Block #1) moves in arbitrary combination of translational and rotational motions such as surge, sway, heave, roll, pitch, and yaw. The body grid with one block is utilized in laminar flow. However, in order to capture thin boundary layer for turbulent flow case, matched grid block is combined. The moving body block has a dense grid near the body, around the corner of the geometry, and near the free surface. This body grid is embedded in a rectangular grid (Block #2) which covers the middle part of wave tank. The rest of the computational domain are covered by two rectangular blocks (#3 and #4) which overlap with the Block #2. Expansion grids were used in Blocks #3 and #4, while Block #2 has uniform grid distribution in horizontal direction. Blocks #2 through #4 have dense grids near the free surface and coarse grids at the bottom. Fig. 3 shows the generation of the chimera grid system for large rolling motion.

All solution-adaptive grids are generated using Vinokur (Vinokur, 1983) distriution and transfinite interpolation (Fletcher, 1991). Each individual grid in chimera grid system can be adjusted and regridded independently without affecting other grids. After adaptive regridding, the PEGSUS program (Fletcher, 1991) was employed to calculate the new interpolation information between the wave tank and body grid blocks

Since each grid block can be moved and resplined in arbitrary manner, it is possible to select the most appropriate grid for each computational block to provide accurate and efficient resolution of the entire flow field. Horizontally expanded wave tank grids are utilized with the damping zone (Park, 1993) to reduce possible wave reflection at the far field. The filtering (Miyata, 1987) is applied to the free surface side of the moving grid block (Block #1 in Fig. 2) where the extreme oscillation of the wave elevation is expected. For the fully nonlinear wave simulations considered here, the numerical grids within each computational block were updated each time.

The overall numerical solution is completed by the hybrid

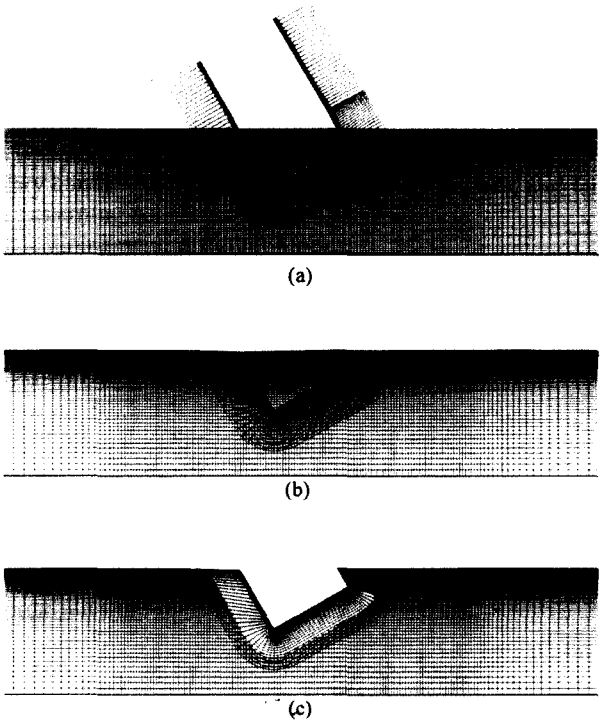

Fig. 3 Chimera grid system for large rolling motion
(a) with baseline grid (b) with physical grid
(c) complete chimera grid

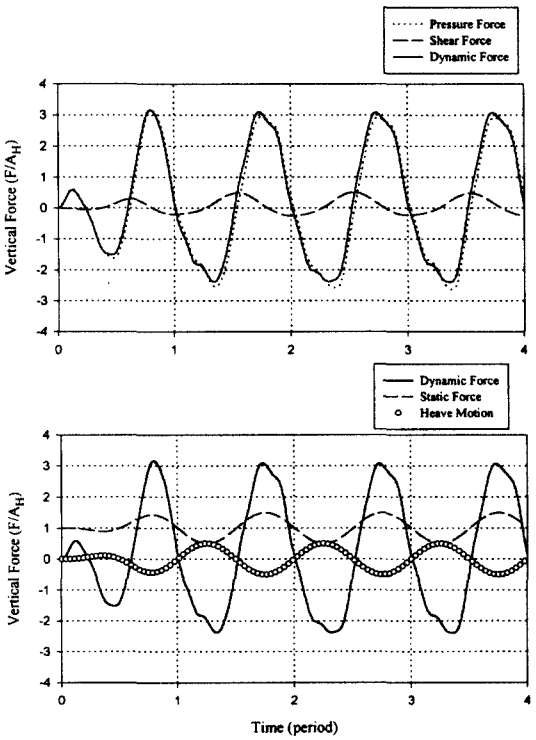

Fig. 4 Vertical force on a heaving body; viscous flow Re =1000 at A_H =0.5 and $\sigma_H^* = \sqrt{2}$

SIMPLER/PISO pressure solver of Chen and Patel (Chen, 1988) and Chen and Korpus (Chen, 1993) which satisfies the equation of continuity at each time step. More detailed descriptions of the Chimera RANS/free surface method were given in Chen, Chen and Davis (Chen, 1997) and Kang (Kang, 1998).

The most obvious advantage of using the Chimera method is the ease with which the grid system is produced. Separate, independent grids can be generated for each component of a complex configuration. Breaking down the flow domain around complex configuration results in multiple grids with simple geometry. Once the Chimera grid system is established, the solution can be obtained with separate grid block, whose accompanying data can be exchanged among grid blocks.

The solution procedure consists of an outer loop over time and inner loops or sweep that iterates over the blocks of the grid. The system of discretized equations generated for each block is solved using an iterative ADI scheme. The solution procedure of RANS method for unsteady problems involving grid movements can be generalized as follows:

1. Construct the grids for each component of the configuration.
2. Determine interpolation information for linking grids using the PEGSUS program.
3. Specify the time dependent input conditions for velocity, pressure, and turbulence fields for the viscous flow.
4. Apply boundary conditions including FSDBC, body, bottom, and far field.
5. Solve RANS governing equations for each blocks.
6. Data communication among different blocks.
7. Iterate steps 4 to 6 until satisfying convergence criteria.
8. Find new free surface using FSKBC.
9. Move the body to the new position and calculate the body velocities.
10. Return to the first step until the maximum time is reached.

4. Results and Discussion

Calculations have been performed for prescribed translational and/or rotational motions. The non-dimensional frequency σ_Φ^* is used in the current prescribed body motion such as heave and roll.

$$\sigma_\Phi^* = \sigma_\Phi \sqrt{\frac{L}{g}} \tag{20}$$

In the dimensional frequency σ_Φ, Φ indicates motions, namely heave (H) and roll (R) in two-dimensional motion. g is gravitational acceleration. The characteristic length L uses either L_B (half beam for heave) or L_d (draft for roll). Heave motion of the floating body is investigated with the laminar flow, while roll motion is investigated boat laminar and turbulent flows. More grid points and more grid blocks are utilized in the turbulent flow than the laminar flow. The aspect ratio of the rectangular body is $B/D=2$. Here, B and D are beam and draft of the body, respectively. The radius of the rounded edge is equal to 5% of the half-beam.

In the present study, the modulation function (Boo et al., 1994) is applied to get smooth variation of the body motion:

$$f_m = \begin{cases} 0.5\times[1-\cos(\pi t/T_m)] & \text{when } t \le T_m \\ 1 & t > T_m \end{cases} \tag{21}$$

T_m is the period of the modulation function.

4.1 Heave Motion

At first, nonlinear calculations are preformed for a heaving body at A_H=0.5, $\sigma_H^* = \sqrt{2}$, and a Reynolds number of 1000. The vertical displacement (Z_H) of the heaving body is prescribed by

$$Z_H = A_H \sin(t) \tag{22}$$

Here, A_H is the dimensionless heaving amplitude which is the actual heaving amplitude a_H divided by the half beam of the body ($A_H = a_H / L_B$). The small heave motion with A_H=0.1 is successfully simulated and shown in Kang (Kang, 1998) and those results are not repeated in the current study. The single 65×30 moving body grid is embedded in a 65×51 rectangular grid that covers the middle part of wave tank. The rest of the computational domain are covered by two 54×51 rectangular grid blocks which overlap with the middle part of grid block.

Upper figure in Fig. 4 shows the time series of pressure and shear forces. It is seen that the force time series are deformed possibly due to strong non-linearity. Lower figure in Fig. 4 shows the dynamic and static forces compared with the sinusoidal heave motion. It is simply concluded that the static forces can be less than dynamic force on large body motion such as A_H =0.5.

Figs. 5(1)~5(6) show the computed velocity vectors and corresponding vorticity ($\nabla\times\mathbf{V}$) contours at $t/T_H = 1.0$ through $t/T_H = 4.0$. Here, T_H is the heave period. The time step in the current study is $\Delta t = T_H/800$. The modulation function is applied up to $T_m = T_H$ for smooth body movement. The dotted lines in the vorticity contour show the negative vorticity that indicates clockwise flows, and the solid lines show the positive vorticity. It is seen that both the velocity vectors and vorticity contours are symmetric with respect to the vertical plane.

Fig. 5(1) shows the fluid circulation below the body bottom at

$t/T_H = 1.0$. At this time, the modulation period has been finished for smooth variation of fluid momentum near the body. Due to both sides of body wall and no-slip condition, the fluid vortex is shown even if the size is small. But, at $t/T_H = 1.25$ as shown in Fig. 5(2), it is seen that the circulation of the fluid grows up below the bottom of the body. At $t/T_H = 1.5$ in Fig. 5(3), during the downward body motion, the fluid below the body bottom was pushed away from the bottom and forced to move upward. This upward flow coupled with downward flow adjacent to the body produces a re-circulating flow. Due to the circulating flow and viscosity of the fluid, a pair of secondary vortices are generated next to the primary circulating flow. At $t/T_H = 1.75$ in Fig. 5(4), the body reached the lowest position but the fluid near body continued to move downward while the primary vortices evolve into narrow and elongate vortices around the side walls. At $t/T_H = 2.0$ in Fig. 5(5), the fluid outside the viscous boundary layer continued its downward motion and moved gradually toward the center to fill the void created by the upward body motion. It is seen that new pairs of vortices are generated above the previous vortices, which was located below the bottom of the body. At $t/T_H = 4.0$ in Fig. 5(6), the results after four cycles of simulations are similar to those observed at $t/T_H = 2.0$. However, it is seen that vortices are shedding away from the both sides of body. This vortex shedding effect may make strong nonlinear fluid and associated wave.

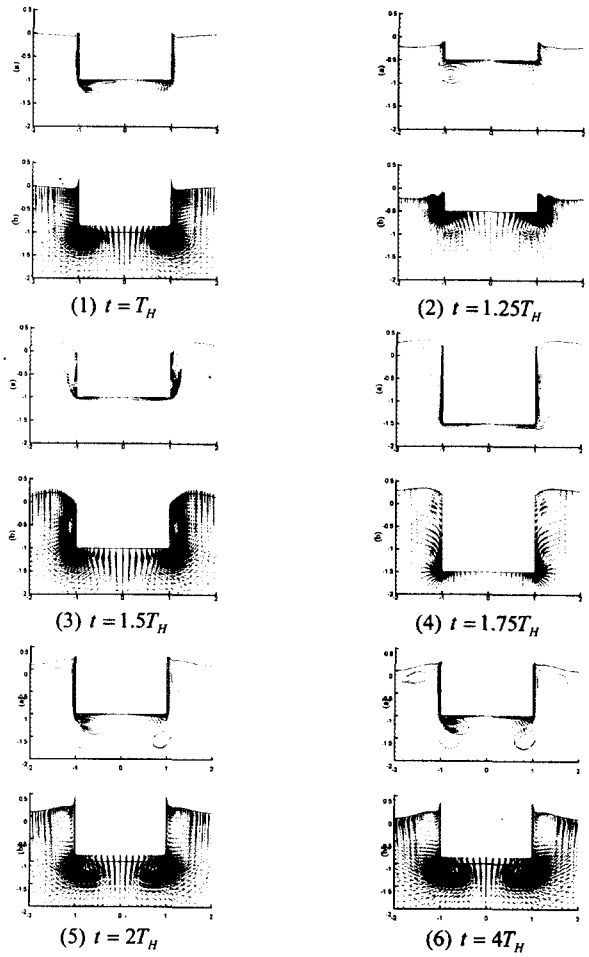

Fig. 5 Heaving body with Re=1000, A_H=0.5, and $\sigma_H^* = \sqrt{2}$
(a) Vorticity contour (b) Velocity vector

4.2 Roll Motion

In addition to the heave motion presented here, the same Chimera RANS method has also been employed for simulation of rolling body motions. The small amplitude of roll motion is shown in Kang and Chen (Kang, 1997) and Chen, Kang, and Huang (Chen, 1998), and the large motion is investigated in the current study.

The body in roll motion has following angular displacement θ_R.

$$\theta_R = A_R \sin(\sigma_R t) \tag{23}$$

where σ_R is roll frequency (rad/sec) and A_R is roll amplitude. The reference velocity is defined by maximum roll velocity.

$$U_0 = L_d \left.\frac{d\theta_R}{dt}\right|_{\max} = \sigma_R A_R L_d \tag{24}$$

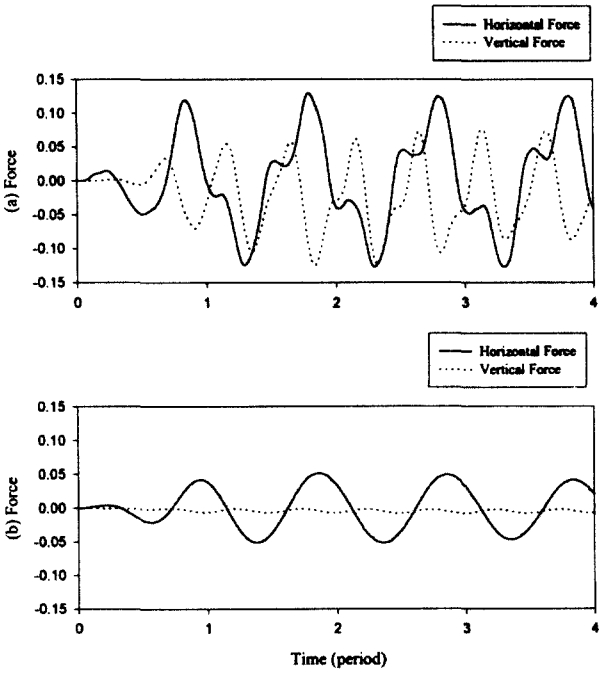

Fig. 6 Force time series for rolling body with $A_R = 30^0$
(a) Viscous flow (Re=1000000) (b) Potential flow

where L_d is draft. The Reynolds number in roll motion is defined by

$$Re = \frac{U_0 L_d}{\nu} = \frac{\sigma_R A_R L_d^2}{\nu} \tag{25}$$

The rolling motions with large rolling amplitudes of $A_R = 20^0$ and $A_R = 30^0$ have been carried out using $Re = 1000$ and $Re = 1000000$. The frequency of σ_R^*=0.25 is used for all simulation. For the laminar flow case, the whole grid system consists of four blocks of grids; one is a moving body grid block, the others are wave tank grid blocks. The 91×40 moving body grid is embedded in a 121×81 rectangular grid that covers the middle part of wave tank. Two 51×81 rectangular blocks cover the rest of the computational domain. For the turbulent flow simulation, the body grid is subdivided into two smaller grid blocks of 91×20 and 91×40. These grids facilitate the implementation of two-layer turbulence model.

The time step is reduced to $\Delta t = T_R / 1600$ and the modulation function is applied up to $T_m = T_R$ for smooth body movement. The center of rotation is changed to the intersection of the half draft and the vertical plane of symmetry for more realistic roll motion of the body. To avoid possible fluctuations of the free surface fluid near the body, the five-point filtering (Miyata, 1987) is applied every other time step.

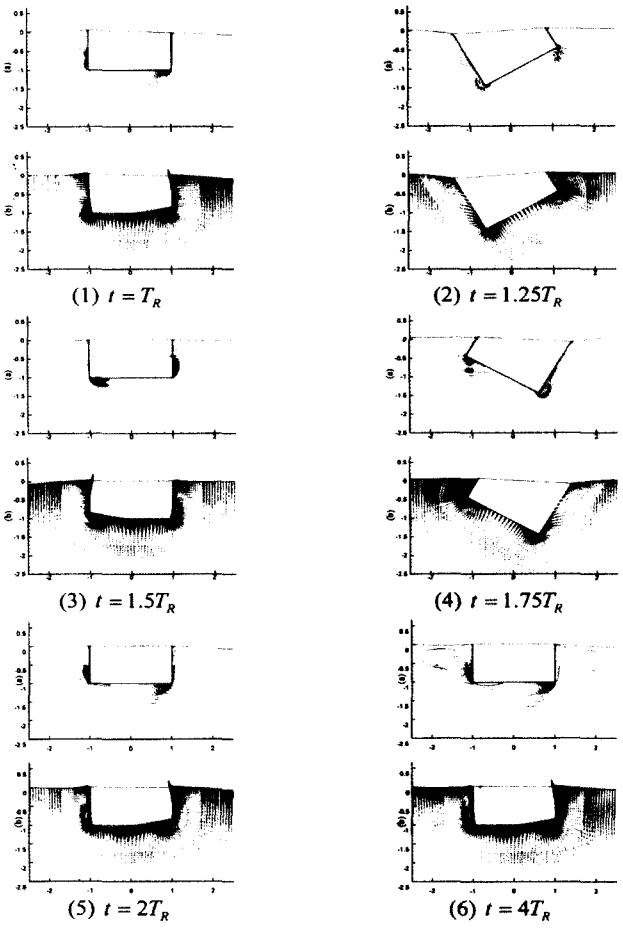

Fig. 7 Rolling body with Re=1000000, $A_R = 30^0$, and σ_R^*=0.25
(a) Vorticity contour (b) Velocity vector

Fig. 6 shows time series for horizontal and vertical forces using viscous and inviscid flow theory. The potential flow simulation is explained in Kang (Kang, 1998) in detail. The potential solver shows the single sinusoidal force time series in Fig. 6(b), while the RANS solver no longer shows single sinusoidal in Fig. 6(a) even if the body is undergoing sinusoidal motion. This may be due to the severe vortex shedding around the rolling body. It is also seen that the period of horizontal force is twice of the period of vertical force.

Figs. 7(1)~7(6) show the computed velocity fields and corresponding vorticity contours at $t/T_R = 1.0$ through $t/T_R = 4.0$ after modulation period $(T_m = T_R)$ using the turbulent flows at Re =1000000. Simulation plots just after modulation period is shown in Fig. 7(1). In this period, even the body motion is small, the vortex can be seen around bottom corner of the rolling body due to viscosity of the fluid. It is interesting that the secondary pair of vortex have been already appeared in opposite rotation next to primary vortex.

In Fig. 7(2), two vortices are formed at bottom right corner and left wall when the body motion has stopped completely at $t/T_R = 1.25$. The body rolls in the counterclockwise direction, while the fluid around the corners rotates in the clockwise direction due to shear stress on the body. The vortices are much stronger than those observed in previous small amplitude motion of the body with $A_R = 5^0$ (see Kang(Kang, 1998)). In Fig. 7(3), the body rolls back in the clockwise direction to the equilibrium position at $t/T_R = 1.5$, and the angular velocity reached maximum values. Both vortices are moved to the opposite sides when comparing with $t/T_R = 1.25$ instant: one moves from bottom right corner to the right wall, the other moves from left wall to the bottom left corner. In addition to the primary vortices around the body corners, the secondary swirling flows are also observed near the middle of the side walls. In Fig. 7(4), the body came to stop at $t/T_R = 1.75$. Even if the fluid on the body has no motion due to the no-slip condition on the body surface, the fluid near the body continues to move in the clockwise direction due to the fluid inertia. In Fig. 7(5), the body rolls to the equilibrium position in the counterclockwise direction at $t/T_R = 2$, and the angular velocity reached maximum values. It can be seen that both vortices move to the other sides: one moves from right wall to bottom right corner, the other moves from bottom

left corner to the left wall. In Fig. 7(6), the vortices at $t/T_R=4$ are stronger than those observed at $t/T_R=2$. From the vorticity contours, several vortices have been generated and shedded away from the body. This clearly indicates that the large roll motion of the body provides energy to keep the vortex shedding in the flow field.

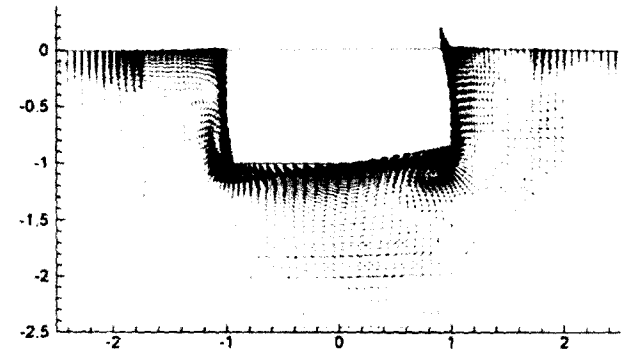

Fig. 8 Velocity vectors around a rolling body at $t=4T_R$ with Re=1000000, $A_R=20^0$, and σ_R^*=0.25

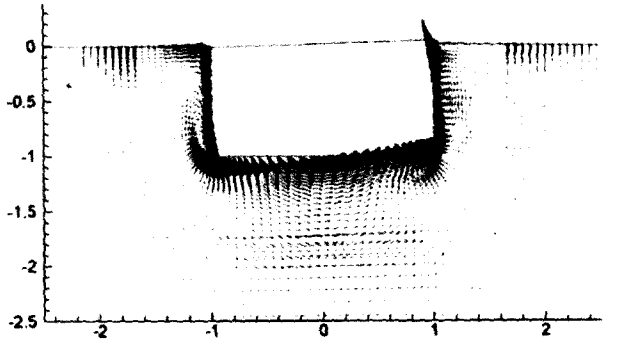

Fig. 9 Velocity vectors around a rolling body at $t=4T_R$ with Re=1000, $A_R=30^0$, and σ_R^*=0.25

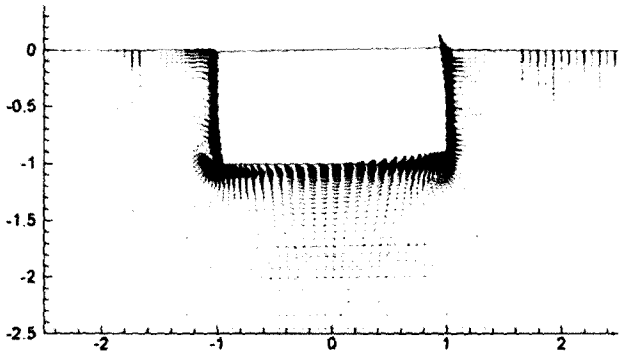

Fig. 10 Velocity vectors around a rolling body at $t=4T_R$ with Re=1000, $A_R=20^0$, and σ_R^*=0.25

In order to examine the influences of Reynolds number and rolling amplitude, more calculations are also performed for =1000000 with $A_R=20^0$, $Re=1000$ with $A_R=30^0$, and $Re=$ 1000 with $A_R=20^0$ as shown in Figs. 8~10. From Fig. 7(6) and Fig. 8 (for $Re=1000000$) as well as Fig. 9 and Fig. 10 (for $Re=$ 1000), it is shown that the vortices using roll motion of $A_R=30^0$ are much stronger than ones using $A_R=20^0$. In addition, Fig. 7(6) and Fig. 9 (for $A_R=30^0$) as well as Fig. 8 and Fig. 10 (for $A_R=20^0$), it is indicated that the fluid from roll motion of $Re=$ =1000000 has more momentum and less viscosity to push vortex away than $Re=1000$. All of these figures clearly indicates that the higher Reynolds number and the larger roll amplitude produces much bigger shear stress and normal pressure forces with stronger vortices near the body corners.

5. Summary and Conclusions

A zonal approach of Chimera RANS numerical method has been described and utilized for the prediction of the rotational viscous fluid behavior. The fluid flow is caused by the oscillating body with large heave and roll motions. The RANS method solves the important viscous flow phenomena such as boundary layers, body-induced vortices, and the nonlinear waves around the body boundary.

Calculations performed by a two-dimensional ship hull in prescribed heave and roll motions clearly demonstrated the strong capability of the Chimera RANS method for propagation of rotational vortices around oscillating bodies. The rotational viscous flow behavior around the oscillating body has been observed in terms of velocity vector and vorticity contour. It is investigated from relative magnitude of velocity vector and vorticity contour that the higher Reynolds number and the large amplitude of heave and roll motions produce much bigger shear stress and normal pressure forces with stronger vortices near the body corners.

In actual sea environments, the heave and roll excitation is not periodic. Current method can be used non-sinusoidal oscillating motion and randomly oscillating motion and can be used for realistic simulation. Based on large motion of body, it is believed that current method can extend green water and capsizing of the oscillating ship body. With some modifications, the method can be readily extended for time-domain simulations of a practical three-dimensional body motion with six-degree of freedom.

Acknowledgment

This work was supported by the Office of Naval Research, Naval Exploratory Development Program in Facilities, under

Contract No. N47408-95-C-0237. Most of the computations were performed on Cray J-90 at the Texas A&M University Supercomputer Center, and the Cray C-90 of Cray Research Inc. at Eagen, Minnesota under the sponsorship of Mr. Chris Hempel.

References

(1) Chen, H.C. "Submarine Flows Studied by Second-Moment Closure," Journal of Engineering Mechanics, Vol. 121, No. 10, pp. 1136~1146, 1995.

(2) Wu, Chun-fa. "Wave-Viscosity Interaction for Bodies in a Free Surface," Ph.D Dissertation, Dept. of Naval Arch. & Offshore Engrg., Univ. of Calif., Berkeley, 142pp, 1990.

(3) Yeung, R.W and Wu, C.F. "Viscosity Effects on the Radiation Hydrodynamics of Two-Dimensional Cylinders," OMAE-Volume I-A, offshore Technology, ASME, pp 309~316, 1991.

(4) Isaacson, Michael and Cheung, K.F. "Second-order wave diffraction around two-dimensional bodies by time-domain method," Applied Ocean Research, 13, 4, 175~186, 1991.

(5) Isaacson, Michael and Cheung, K.F. "Time-domain second-order wave diffraction in three dimensions," Journal of Waterway, Port, Coastal and Ocean Engineering, ASCE, 118, 5, 496~516, 1992.

(6) Isaacson, Michael and Ng, Joseph Y.T. "Time-Domain Second-Order Wave Radiation in Two Dimensions," Journal of Ship Research, Vol. 37, No. 1, March, pp 25~33, 1993.

(7) Taneda, Sadatoshi. "Visual observations of the flow around a half-submerged oscillating shpere," J. Fluid Mech., vol. 227, pp 193~209, 1991.

(8) Yeung, R.W. and Ananthakrishnan, P. "Oscillation of a Floating Body in a Viscous Fluid," Journal of Engineering Mathematics, Vol. 26, No. 1, pp 211~230, 1992.

(9) Liaw, C.Y., Bishop, S.R. and Thompson, J.M.T. "Heave-Excited Rolling Motion of a Rectangular Vessel in Head Seas," International Journal of Offshore and Polar Engineering, Vol. 3, No. 1. pp 26~31, 1993.

(10) Chen, H.C., Kang, C.H. and Huang, E.T. "Time-Domain Simulation of Ship Roll Motions by a Chimera RANS Method," 12th ASCE Engineering Mechanics Conference, La Jolla, CA, May 17-20, 1998.

(11) Chen, H.C. and Patel, V.C. "Near-Wall Turbulence Models for Complex Flows Including Separation," AIAA Journal, Vol. 26, No. 6, pp 641~648, 1988.

(12) Chen, H.C. and Patel, V.C. "The Flow Around Wing-Body Junctions," Proceedings of the 4th Symposium on Numerical and Physical Aspects of Aerodynamic Flows, Long Beach, CA, 16-19 January, 1989.

(13) Chen, H.C., Patel, V.C. and Ju, S. "Solutions of Reynolds-Averaged Navier-Stokes Equations for Three-Dimensional Incompressible Flows," Journal of Computational Physics, Vol. 88, No. 2, pp 305~336, 1990.

(14) Chen, H.C. and Korpus, R. "A Multi-block Finite-Analytic Reynolds-Averaged Navier-Stokes Method for 3D Incompressible Flows," Individual Papers in Fluids Engineering, edited by F. M. White, ASME FED-Vol. 150, pp 113~121, ASME Fluids Engineering Conference, Washington, DC, June 20-24, 1993.

(15) Chen, H.C., Chen, M. and Davis, D.A. "Numerical Simulation of Transient Flows Induced by a Berthing Ship," International Journal of Offshore and Polar Engineering, Vol. 7, No. 4, pp 277~284, 1997.

(16) Kang, C.H. "Simulation of Floating Body Motions by Interactive RANS/LAPLACE Methods," Dissertation, Texas A&M University, College Station, TX, 1998.

(17) Park, J. C., Zhu, M., & Miyata, H. "On the accuracy of numerical wave making techniques," Journal of the Society of Naval Architects of Japan, 173, pp 35~44, 1993.

(18) Vinokur, M. "On one-dimensional stretching functions for finite difference calculation," J. Computational Physics, 50, pp 215~234, 1983.

(19) Fletcher, C. A. J. "Computational techniques for fluid dynamics volume II," Springer-Verlag. Heidelberg, Germany, 1991.

(20) Suhs, N.E. and Tramel R.W. "PEGSUS 4.0 Users Manual," Arnold Engineering Development Center Report, AEDC-TR-91-8, Arnold Air Force Station, TN, 1991.

(21) Miyata, H., Sato, T., & Baba, N. "Difference solution of a viscous flow with free surface wave about an advancing ship," J. Computationl Physics, 72, pp 393~421, 1987.

(22) Kang, C.H. and Chen, H.C. "Interactive RANS/LAPLACE Simulation of Ship Heave, Sway and Roll Motions," COE Report No. 357, 111 pages, Texas Engineering Experiment Station, Texas A&M University, College Station, TX, 1997.